Restoring DIC Microscopy Images from Multiple Shear Directions

Zhaozheng Yin[1]   Dai Fei Elmer Ker[2]   Takeo Kanade[1]

[1]Robotics Institute, [2]Department of Biological Sciences
Carnegie Mellon University, Pittsburgh, US

Abstract. Differential Interference Contrast (DIC) microscopy is a non-destructive imaging modality that has been widely used by biologists to capture microscopy images of live biological specimens. However, as a qualitative technique, DIC microscopy records specimen's physical properties in an indirect way by mapping the *gradient* of specimen's optical path length (OPL) into the image intensity. In this paper, we propose to restore DIC microscopy images by quantitatively estimating specimen's OPL from a collection of DIC images captured from multiple shear directions. We acquire the DIC images by rotating the specimen dish on the microscope stage and design an Iterative Closest Point algorithm to register the images. The shear directions of the image dataset are automatically estimated by our coarse-to-fine grid search algorithm. We develop a direct solver on a regularized quadratic cost function to restore DIC microscopy images. The restoration from multiple shear directions decreases the ambiguity among different individual restorations. The restored DIC images are directly proportional to specimen's physical measurements, which is very amenable for microscopy image analysis such as cell segmentation.

1 Introduction

Under a traditional brightfield microscope, living specimens such as cells are colorless and transparent because they are predominantly phase objects that absorb and scatter little illumination light. That is, cells do not significantly alter the amplitude of the light waves passing through them and as a result, produces little or no contrast when viewed under a brightfield microscope. For tissue culture cells, a cell's optical path length (OPL, product of its refractive index and geometric thickness) is normally different from that of the surrounding medium (about $0.125\mu m$ or a quarter wavelength of green light). This optical path difference induces a small phase difference between the light waves passing through cells and those traversing the surrounding medium. Since human eyes are sensitive to amplitude differences between light waves as opposed to phase differences, Differential Interference Contrast (DIC) microscopy technique was invented in 1950s to convert these minute phase variations to intensity changes that can be easily detected by human eyes (see textbook [12]).

The DIC microscope works by splitting a polarized illumination light wave into two component waves that are spatially displaced (sheared) along a specific direction, and then recombining the two waves after they travel through adjacent locations on the

specimen plate. The recombination (interference) is sensitive to phase variations between the two component waves. An adjustable bias (bias retardation) can be added into the phase variation. Because the phase variation between the two waves is caused by OPL difference at two adjacent locations, this microscopy imaging technique is then called "differential interference," and the observed intensity in DIC images is proportional to the OPL *gradient* along the shear direction. The relief-like images generated by DIC microscopy have the pseudo 3D shadow-cast effects as if the specimens are illuminated from an oblique lighting resource (e.g. Fig. 1(a,b)), but this artifact only indicates the orientation of a specimen's OPL gradient rather than the real topographical structure.

1.1   Related Work

Since the intensity of a DIC image is not a linear mapping of specimen's inherent properties such as refractive index, thickness or OPL, this has triggered strong research interest in reconstructing the original physical properties of specimens from DIC images. We summarize the related work in three aspects: hardware-related techniques, reconstruction from a single DIC image and reconstruction using multiple DIC images.

(1) Arnison et al. [1] proposed a hardware extension to the conventional differential interference by inserting an extra quarter wave plate in the optical layout of a DIC microscope, and restored the phase objects by varying bias setting and using geometric phase-shift techniques. Shribak et al. [15] developed an orientation-independent DIC microscopy by adding liquid crystal devices in the common DIC microscopes. The setup of these new optical configurations might be complicated and inaccessible to the common biology labs.

(2) Noticing the gradient interpretation of DIC images, line integration methods were developed to reconstruct DIC images [8]. The line-by-line integration along shear direction introduces new streaking artifacts in reconstructed images and it is sensitive to gradient noise, thus Hilbert transform [2] and other ad hoc techniques such as low-pass filtering [7] were explored to reduce the streaking artifacts to a certain degree. General image processing algorithms such as deconvolution by Wiener filter [7, 11] or by Landweber iterations [6] have been applied to reconstruct optical path length from DIC images. A preconditioning approach was recently proposed in [10] where the DIC image is reconstructed by minimizing a nonnegative mixed-norm constrained cost function. We reimplemented these three types of approaches and applied them on a pair of DIC images of the same specimens captured from two different shear directions. As shown in Fig. 1(c) and (d), we can observe the streak artifacts by line integration. Fig. 1(e) and (f) show the unsatisfactory restoration results by Wiener filtering with 1% noise-to-signal power ratio of the additive noise. The deconvolution performance depends on the prior knowledge of various hardware parameters (such as shear directions and bias setting) and image noise models. Fig. 1(g) and (h) show the reconstruction results by the preconditioning method. It is time-consuming to estimate the direct measurement on specimens by the iterative preconditioning method.

From Fig. 1, we have a common observation that the reconstructions of the image pair (Fig. 1(c,d), Fig. 1(e,f), and Fig. 1(g,h)) are not the same for the same specimens. That is, when biologists analyze specimens, they will obtain different measurements
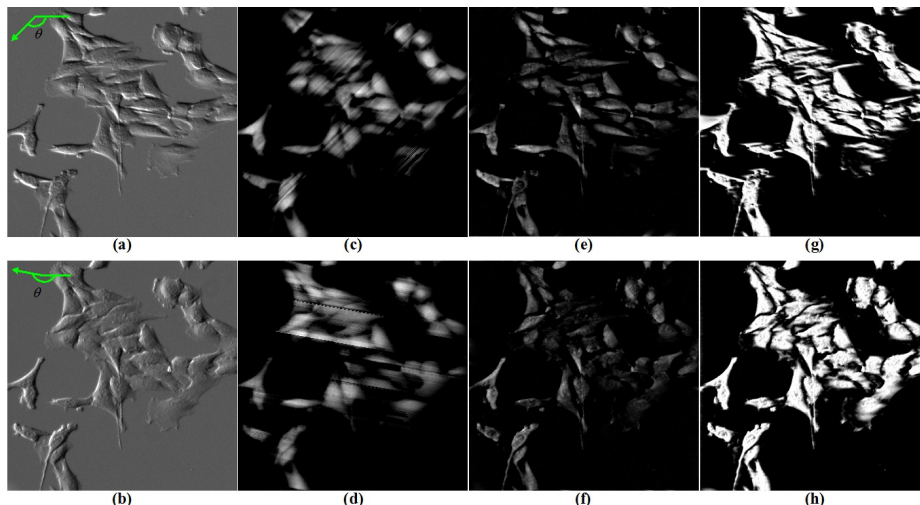
Fig. 1. Reconstructing optical path length from DIC images. (a,b) Two DIC image of the same specimens captured from two different shear directions (the arrow denotes the shear direction θ); (c,d) Reconstruction by line integration enhanced by low-pass filtering; (e,f) Reconstruction by deconvolution (Wiener filtering); (g,h) Reconstruction by preconditioning.

on the specimen's optical path length according to different shear directions. This is very undesirable because biologist don't know which direction-specific reconstruction unveils the real properties of specimens.

(3) A few approaches have been proposed to restore specimen's properties from multiple DIC images [1, 6, 9, 13, 15]. These approaches either rotate prisms, change bias settings or step the shear azimuth to capture multiple DIC images, and they require at least two images captured from a pair of orthogonal shear directions. Without specially-designed hardware, it is hard to rotate the specimen dish or prism manually by exact 90 degrees to satisfy the orthogonal requirement.

1.2   Our Proposal

We propose a novel approach to restore DIC microscopy images captured from multiple shear directions without the strict orthogonal requirement. In Section 2, we derived a closed-form solution for the restoration. Since the DIC images were captured by manually rotating the dish on the stage of a common DIC microscope, there are Euclidean transformation (rotation and translation) among captured DIC images. We designed an Iterative Closest Point (ICP) algorithm to register the image dataset (Section 3). Rather than measuring the shear directions of the DIC images manually, we propose a coarse-to-fine grid search algorithm to find the shear directions automatically (Section 4). We show our experiment results in Section 5 with the conclusion followed in Section 6.

2   Problem Formulation and Restoration Method

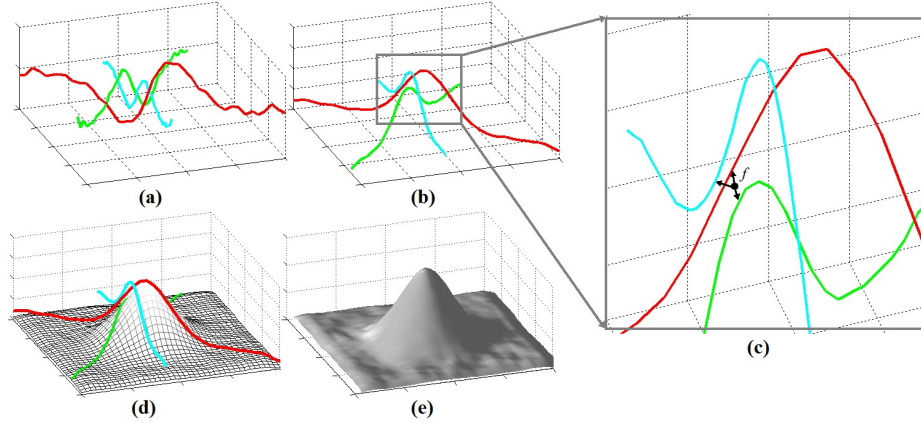Based on the gradient interpretation of DIC images, we have the following simplified DIC imaging model

Fig. 2. Estimate the optical path length in DIC images. (a) The three observed gradient signals along different shear directions; (b) The three signals after integration do not intersect in the OPL space (i.e. there is no consensus among the restored signals); (c) We propose to restore DIC images (i.e. estimate the optical path length) by minimize the total distance to all integrated signals; (d) The spatial smooth constraint (gray mesh) is considered during the restoration; (e) The restoration result using three DIC images.

$$\mathbf{g} = \nabla_\theta \mathbf{f} \tag{1}$$

where $\mathbf{g}(u, v)$ is an observed DIC image[1], ∇_θ is the gradient operator along the shear direction θ and $\mathbf{f}(u, v)$ is the DIC image to be restored. This imaging model is also used by some other DIC reconstruction methods such as the iterative preconditioning method [10] and deconvolution by Landweber iteration [6]. More accurate and complicated DIC imaging models can be referred to [14].

Based on Eq.1, the DIC image can be restored by applying line-by-line integration on the observed gradient $\mathbf{g}$ along the shear direction θ

$$\mathbf{f} = \int \mathbf{g} \, d\mathbf{x}^\theta \tag{2}$$

where $\mathbf{x}^\theta$ denotes a location on the lines along the shear direction. For a line on the specimen plate with M locations, we can observe $M - 1$ gradient values by DIC microscopy. The line integration method reverses the differential problem by estimating the OPL values at M locations from observed $M - 1$ gradient values, thus there are more unknowns than available equations. The under-constrained equation system plus the image acquisition noise may make the restored signal inconsistent when we perform line integration along different shear directions. As shown in Fig. 2(a), at a specimen location, three gradient signals are extracted from three DIC images along their shear directions. When we integrate the three gradient signals independently (Fig. 2(b)), the three reconstructed signals do not intersect in the OPL space - they have different restoration values on $\mathbf{f}$ at the same specimen location! To avoid the ambiguity and achieve the consensus among different restorations, we propose to estimate the true $\mathbf{f}$

---

[1] We drop the 2D location indices (u, v) in all the equations for concise expressions.

in a least-square sense. In other words, the real $\mathbf{f}$ at that location should have the minimum total distance to all integrated signal curves (Fig. 2(c)). Thus, we are looking for an image $\mathbf{f}$ to minimize

$$\sum_{i=1}^{K} \int_{\mathcal{R}^2} (\mathbf{f} - \int \mathbf{g}_i \, d\mathbf{x}^{\theta_i})^2 d\mathbf{x} \tag{3}$$

where i indexes the K DIC images captured from different shear directions θ_i on the same specimens, $\mathbf{x} = (u, v)$ is a pixel location on the 2D Euclidean space $\mathcal{R}^2$. The minimization on Eq. 3 needs to carry out the line integration $\int \mathbf{g}_i \, d\mathbf{x}^{\theta_i}$ explicitly for each DIC image. However, the line integration itself is not a satisfactory restoration as we see in Fig. 1(c) and (d). Instead, we propose to restore $\mathbf{f}$ by minimizing a cost function in the gradient domain directly

$$\sum_{i=1}^{K} \int_{\mathcal{R}^2} (\nabla_{\theta_i} \mathbf{f} - \mathbf{g}_i)^2 d\mathbf{x}. \tag{4}$$

The goal is to compute an $\mathbf{f}$ whose gradients along different shear directions are as close as possible to the corresponding given gradients, $\mathbf{g}_i$'s. After mapping the pixel location from 2D Euclidean space to a new surface defined by the K shear directions

$$\{\mathbf{x} = (u, v), \mathbf{x} \in \mathcal{R}^2\} \rightarrow \{\boldsymbol{\theta} = (\theta_1, \theta_2, \cdots, \theta_K), \boldsymbol{\theta} \in \Theta\} \tag{5}$$

and using the commutativity of $\sum$ and $\int$ operations, the cost function (Eq. 4) is converted into

$$\int_{\Theta} \sum_{i=1}^{K} (\nabla_{\theta_i} \mathbf{f} - \mathbf{g}_i)^2 d\boldsymbol{\theta}. \tag{6}$$

Eq. 6 only measures the fidelity of the restoration to all the observed data. We enhances the data fidelity with smooth and sparse regularizations and propose the following objective function for restoration

$$O(\mathbf{f}) = \int_{\Theta} \left[\left(\sum_{i=1}^{K} (\mathbf{d}_{\theta_i} * \mathbf{f} - \mathbf{g}_i)^2 \right) + \omega_s (\mathbf{a} * \mathbf{f})^2 + \omega_r \mathbf{f}^2 \right] d\boldsymbol{\theta} \tag{7}$$

where $\mathbf{d}_\theta$ is a differential kernel along the shear direction θ, "*" is the convolution operation, $\mathbf{d}_{\theta_i} * \mathbf{f}$ is equivalent to $\nabla_{\theta_i} \mathbf{f}$, $\mathbf{a}$ is a kernel for local smooth, ω_s and ω_r are weighting coefficients for the smooth and sparse regularizations, respectively. $\mathbf{d}_{\theta_i}$ can be defined by a directional first-derivative-of-Gaussian kernel [10]. The smooth constraint encourages nearby pixels to have the same restoration values (Fig. 2(d)). For example, we can regularize a restored pixel value to be close to the average of its neighboring pixels (i.e. $\mathbf{a} = [1\ 1\ 1;\ 1\ -8\ 1;\ 1\ 1\ 1]/8$ for 8-connected neighborhood). The l_2 sparse regularization penalizes large $\mathbf{f}$ values and enforces the restored background pixels (with equal OPL at adjacent locations) to be close to zero. A stronger sparse regularization is using l_1 norm but there is no closed-form solution for that. More discussions on the regularizations can be referred to the rich research work on compressive sensing [3].

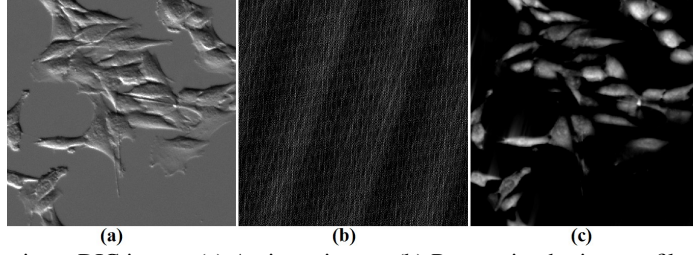The solution that minimizes Eq. 7 must satisfy the Euler-Lagrange equation

Fig. 3. Restoring a DIC image. (a) An input image; (b) Restoration by inverse filtering; (c) Our restoration by minimizing a regularized cost function.

$$\frac{\partial \mathbf{E}}{\partial \mathbf{f}} - \sum_{i=1}^{K} \frac{\partial}{\partial \theta_i} \frac{\partial \mathbf{E}}{\partial \mathbf{f}_{\theta_i}} = 0 \tag{8}$$

where $\mathbf{f}_{\theta_i}$ is a shorthand notation of $\mathbf{d}_{\theta_i} * \mathbf{f}$ and $\mathbf{E}$ is the integrand inside Eq. 7

$$\mathbf{E} = \left(\sum_{i=1}^{K} (\mathbf{d}_{\theta_i} * \mathbf{f} - \mathbf{g}_i)^2 \right) + \omega_s (\mathbf{a} * \mathbf{f})^2 + \omega_r \mathbf{f}^2. \tag{9}$$

Substituting $\mathbf{E}$ into Eq. 8 for the differentiating, we have

$$2\omega_s \mathbf{a} * \mathbf{a} * \mathbf{f} + 2\omega_r \mathbf{f} - 2 \sum_{i=1}^{K} \mathbf{d}_{\theta_i} * (\mathbf{d}_{\theta_i} * \mathbf{f} - \mathbf{g}_i) = 0. \tag{10}$$

Now, applying Fourier transform, $\mathcal{F}$, on both sides of this equation, we obtain

$$2\omega_s \mathbf{A}^2 \cdot \mathbf{F} + 2\omega_r \mathbf{F} - 2 \sum_{i=1}^{K} \mathbf{D}_{\theta_i}^2 \cdot \mathbf{F} + 2 \sum_{i=1}^{K} \mathbf{D}_{\theta_i} \cdot \mathbf{G}_i = 0 \tag{11}$$

where $\mathbf{A} = \mathcal{F}\{\mathbf{a}\}$, $\mathbf{F} = \mathcal{F}\{\mathbf{f}\}$, $\mathbf{D}_{\theta_i} = \mathcal{F}\{\mathbf{d}_{\theta_i}\}$, $\mathbf{G}_i = \mathcal{F}\{\mathbf{g}_i\}$, "$\cdot$" denotes the element-wise production and $\mathbf{D}_{\theta_i}^2 = \mathbf{D}_{\theta_i} \cdot \mathbf{D}_{\theta_i}$. Solving Eq. 11 for $\mathbf{F}$, we have

$$\mathbf{F} = -(\sum_{i=1}^{K} \mathbf{D}_{\theta_i} \cdot \mathbf{G}_i)./(\omega_s \mathbf{A}^2 + \omega_r - \sum_{i=1}^{K} \mathbf{D}_{\theta_i}^2). \tag{12}$$

where "./" denotes the element-wise division. $\mathbf{f}$ is then restored by $\mathbf{f} = \mathcal{F}^{-1}\{\mathbf{F}\}$. Fig. 2(e) shows a restored result using three images with different shear directions.

For a single DIC image with shear direction θ, the direct solution is

$$\mathbf{F} = -(\mathbf{D}_\theta \cdot \mathbf{G})./(\omega_s \mathbf{A}^2 + \omega_r - \mathbf{D}_\theta^2). \tag{13}$$

If without regularizations ($\omega_s = \omega_r = 0$), Eq. 13 is degraded into an inverse filtering

$$\mathbf{F} = \mathbf{G}./\mathbf{D}_\theta. \tag{14}$$

However, the simple inverse filtering can not restore a correct DIC image (Fig. 3(b)), which justifies the needs of regularization. As a comparison, our restoration by Eq. 13 with $\omega_s = 0.1$ and $\omega_r = 0.001$ is shown in Fig. 3(c) that is much better than the inverse filtering. Please note that the restoration from a single shear direction (Eq. 13) contains

ambiguity to measure the real specimen property thus we have derived solution (Eq. 12) to restore DIC images from multiple shear directions. Eq. 13 is only used in Algorithm 2 (Section 4) for estimating the shear direction of each individual DIC image.

3   Register a Collection of DIC Images

When capturing a collection of DIC images with different shear directions by rotating and translating dishes, we must register those images such that the same pixel location in the image dataset represents the same specimen sample in the world. Note: this registration step can be waived if there is a DIC microscope with rotatable prisms at hand. We revised the Iterative Closest Point (ICP) idea [4] to register two DIC images. Harris corner detector [5] and local non-max suppression are used to locate corners as feature points for matching in the ICP algorithm. The corners are tolerant to appearance changes in DIC images from different shear directions. However, the ICP algorithm can converge to the optimum only when the initialization (rotation $\mathbf{R}_0$ and translation $\mathbf{T}_0$) is close to the optimum. To find the correct $\mathbf{R}$ and $\mathbf{T}$ to register images, we uniformly sample the entire search space of all possible initializations (e.g. every 30 degrees of rotation and every 100 pixels of translation) and run the ICP algorithm from these initializations to find the global optimal $\mathbf{R}$ and $\mathbf{T}$. The new designed ICP algorithm is summarized below. Fig. 4 shows an registration example using this ICP algorithm.
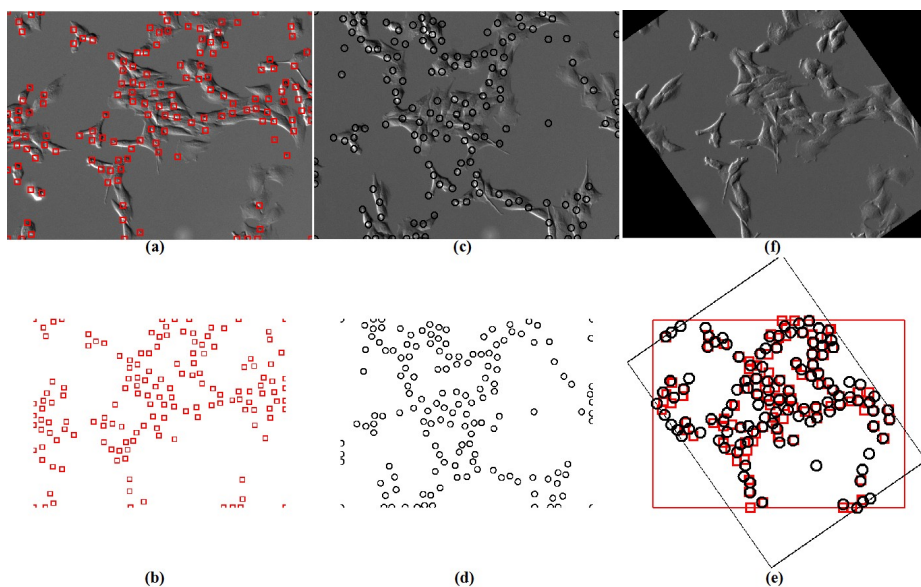

Fig. 4. Register two DIC images by Iterated Closest Point algorithm. (a,b) Image 1 and its corner points (red squares); (c,d) Image 2 and its corner points (black circles); (e) The two groups of corner points are matched with the least total distance cost; (f) The registered image 2 regarding to image 1 based on the Euclidean transformation computed from matched corner points.
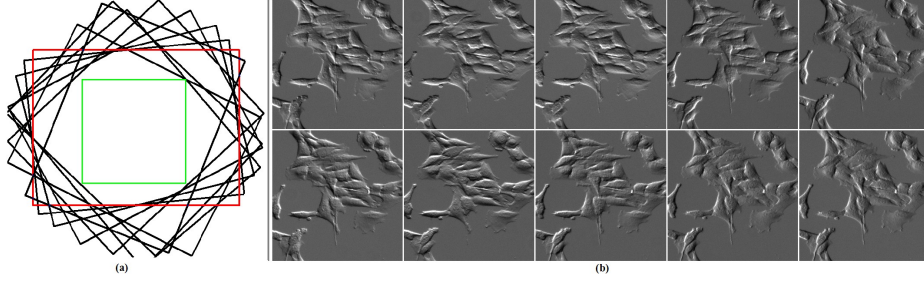
Fig. 5. Register a collection of images and extract the sub-images within the overlapped regions for our analysis. (a): Nine images are registered regarding to the first image. (b) The ten sub-images within the overlapped square regions.

For a collection of DIC images, we randomly pick a reference image and register all the others regarding to it. The registered images overlap in a polygon area and we crop the largest square sub-images from the overlapped region for our analysis (Fig. 5).

Algorithm I: ICP Algorithm to Register Two DIC Images

Extract two groups of corner points $\{\mathbf{Q}_j\}$ and $\{\mathbf{P}_i\}$ from image 1 and image 2, respectively. Compute the centroids: $\bar{\mathbf{P}} = \frac{1}{|\mathbf{P}|}\sum_i \mathbf{P}_i$, and $\bar{\mathbf{Q}} = \frac{1}{|\mathbf{Q}|}\sum_j \mathbf{Q}_j$. Update $\mathbf{P}_i \leftarrow \mathbf{P}_i - \bar{\mathbf{P}}$, $\mathbf{Q}_j \leftarrow \mathbf{Q}_j - \bar{\mathbf{Q}}$.

Initialize $\mathbf{R} = \mathbf{R}_0$, $\mathbf{T} = \mathbf{T}_0$, and $c = 0$.

Repeat the following steps until there is no change on c.

1. Bi-directional Matching: $\forall \mathbf{P}_i$, find the closest $\mathbf{Q}_j$ in the Euclidean space. For $\mathbf{Q}_j$, find the closest $\mathbf{P}_k$. If $i = k$, the two corner points are matched, and update $c+ = |\mathbf{P}_i - \mathbf{Q}_j|$.

2. Transformation: For all matched corner points, compute $\mathbf{W} = \sum_{<i,j>} \mathbf{P}_i \mathbf{Q}_j^T$. Take the singular value decomposition (SVD) of matrix $\mathbf{W}$, $\mathbf{W} = \mathbf{U}\mathbf{\Sigma}\mathbf{V}^T$. Compute the rotation matrix as $\mathbf{R} = \mathbf{V}\mathbf{U}^T$, and the translation vector as $\mathbf{T} = \bar{\mathbf{Q}} - \mathbf{R}\bar{\mathbf{P}}$. $\forall \mathbf{P}_i$, update $\mathbf{P}_i \leftarrow \mathbf{R}\mathbf{P}_i + \mathbf{T}$.

Use the final matched points to compute $\mathbf{R}^*$ and $\mathbf{T}^*$, rotate and translate image 2 regarding to image 1 accordingly.

4   Estimate the Shear Directions

After registration, the shear direction difference between the first image and the other $K - 1$ registered images are actually the rotation angle θ_r^i ($i = 1...K$ and $\theta_r^1 = 0$). In other words, if the shear direction of the first image is θ_s, the shear directions of the rest images are $\theta_s - \theta_r^i$. Since θ_r^i's are already known from the registration step, we only need to estimate a single unknown variable θ_s. As shown in Fig. 6(g), when correct shear directions are estimated for a pair of DIC images, the difference between the two restorations reaches the minimum. We use this fact to estimate the shear direction over the collection of registered images by a fast coarse-to-fine grid search algorithm.

Algorithm II: Coarse-to-Fine Grid Search for Shear Direction θ_s

Initialize $lb = 0$, $ub = 360$ and $\delta_\theta = 30$.

while $\delta_\theta > 1$
    for $\theta_s = lb; \theta_s < ub; \theta_s = \theta_s + \delta_\theta$
        for $i = 1; i < K; i++$
            Solve $\mathbf{f}_i$ with $\theta = \theta_s - \theta_r^i$ through Eq. 13;
        $cost[\theta_s] = \sum_{\substack{i \neq j \\ i,j=1...K}} |\mathbf{f}_i - \mathbf{f}_j|$
    $\theta_s^* \leftarrow \arg\min cost[\theta_s]; \delta_\theta \leftarrow \delta_\theta/4; lb \leftarrow \theta_s^* - 2\delta_\theta; ub \leftarrow \theta_s^* + 2\delta_\theta;$
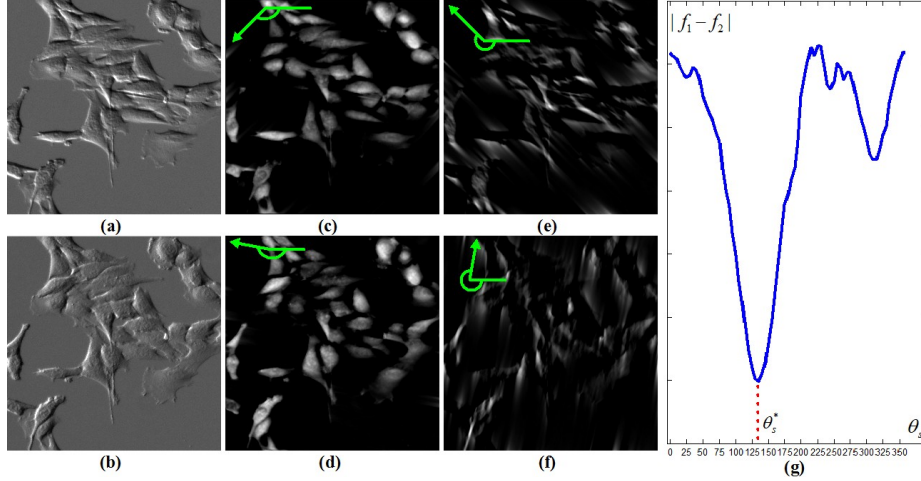Return θ_s^*;

Fig. 6. Estimate the shear direction. (a,b) Image 1 and 2; (c,d) The restorations corresponding to the correct shear directions; (e,f): The restorations corresponding to wrong shear directions; (g) The difference between two restored images is a function of the shear direction.

5   Experiment Results

We captured DIC images from different shear directions by manually rotating the specimen dish on the stage. The collected images are registered automatically by our ICP algorithm and the shear directions of each image is estimated by our coarse-to-fine grid search algorithm.

First, we qualitatively evaluate our restoration results. Fig. 7(a) shows an image (700*700 pixels) on two cells with high magnification. When we apply the direct solver on the captured images individually, we observe different restoration results (Fig. 7(c-h)). The ensemble restoration on the entire collection of images reveals the cells' optical path length much better and has less noise left on the restoration (Fig. 7(b)). Fig. 8 show the other three collections of DIC images we acquired with low magnification and their image restorations. Compared to the independent restorations (e.g. the last two columns of Figure 8), the jointly restored image by an ensemble of DIC images are closer to the physical properties of cells. There is less ambiguity to compute the optical path length in joint restoration than the rotation-variant independent restoration.

To quantitatively evaluate the effect of our restoration results on microscopy image analysis, we apply it onto the cell segmentation task. As we see in the third column
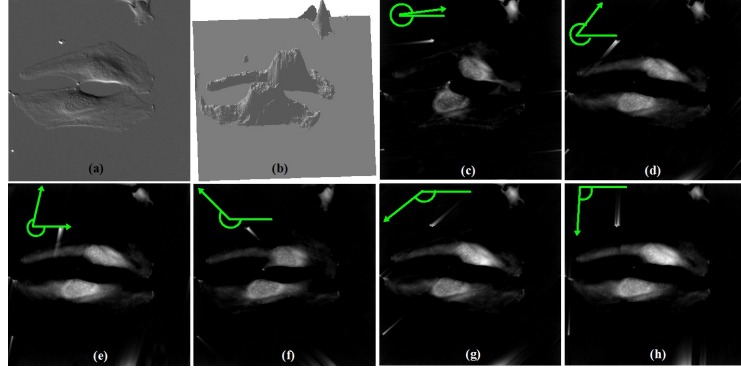
Fig. 7. Reconstructing DIC images. (a) One DIC image of the image collection; (b) The reconstructed OPL from a collection of DIC images (3D surface view); (c-i) The independent restoration from individual DIC images (green arrows denote the shear directions).

of Fig. 8, since the pixel values in the restored images represent the specimen's inherent properties, there is no pseudo 3D shadow-cast effect in the images. In the restored images, cell pixels are always positive against approximately zero background, thus images can be easily segmented by straightforward thresholding for further applications of cell counting, tracking etc., which is not easily possible with original DIC images. We manually label all cell boundaries in each image collection as ground truth masks. After thresholding the restored DIC image to obtain the cell mask, we compare it with the manually-labelled ground truth mask using the accuracy as the evaluation measure

$$\text{ACC} = (|\text{TP}| + |N| - |\text{FP}|)/(|P| + |N|) \tag{15}$$

where cell and background pixels are denoted as positive (P) and negative (N) respectively, true positive (TP) stands for those cell pixels correctly labelled by both human annotator and computer algorithms, and false positive (FP) are those cell pixels classified by computer algorithms mistakenly. We use the same technique in [16] to learn the best threshold for segmentation.

With K DIC images, we pick k ($k = 1...K$) of them as a collection and run our restoration algorithm on this collection. For example, when $k = 1$ we run the restoration algorithm on each single DIC image. When $k = 5$, we pick 5 images from the K DIC images and run the restoration. We exhaustively tested all the possible combinatorial choices, and computed the mean and standard deviation on the accuracy regarding to different image collection sizes. As we see in Fig. 9, there are more ambiguities (the vertical red bar in Fig. 9) among different restoration results when the image collection size k is small. As more images are added into the image collection, the restoration accuracy increases and the ambiguity decreases. The accuracy curve levels off when enough DIC images from different shear directions are included into the image collection. Overall, we achieve the segmentation accuracy of $81\% - 95\%$ on the three collections of DIC images. Difficulties were encountered during the restoration of predominantly flat cells that consequently had low gradient values in the observed DIC images. Less sparsity regularization on these regions may overcome the challenge. We leave the spatially-adaptive regularization in the future work to explore.
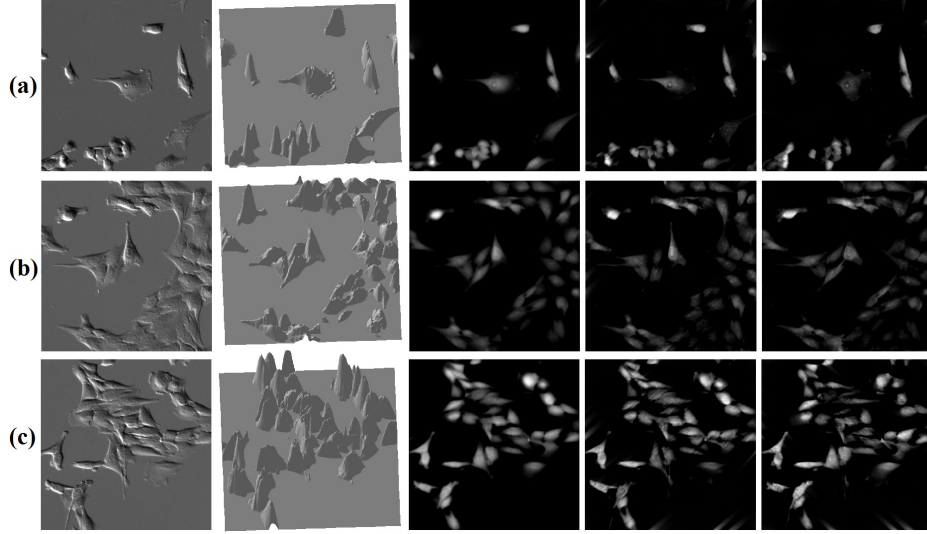
Fig. 8. Restoring DIC images. Column 1: one sample image in each collection; Column 2: the jointly reconstructed OPL (3D surface view); Column 3: The reconstructed DIC images whose intensity values correspond to the reconstructed OPL values; Column 4 and 5: Two independent restorations of DIC images with different shear directions, as comparisons to the ensemble restoration.

6   Conclusions

In DIC microscopy images, the intensity values are proportional to the gradient of specimen's optical path length (OPL). To quantitatively measure specimen's physical properties directly, we propose to restore DIC images from multiple shear directions. The specimen dish is manually rotated to acquire a collection of DIC images with different shear directions. An Iterative Closest Point algorithm is designed to register these images, and the shear directions of the image dataset are automatically estimated by our coarse-to-fine grid search algorithm. We formulate the restoration problem by minimizing a regularized a cost function with a closed-form solution.
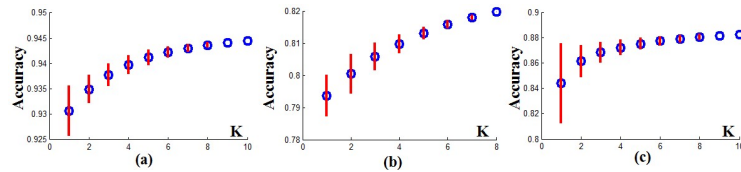

Fig. 9. The mean (blue circle) and stand deviation (red bar) of the segmentation accuracy when using different image collection size k. (a,b,c) are evaluation results from three image datasets corresponding to Figure 8(a,b,c), respectively.

Compared to the reconstruction methods based on a single DIC image which may reconstruct different optical path lengths according to different shear directions, our

method is orientation-invariant. Without the strict requirement of at least two orthogonal shear directions as needed by the previous multiple-image-based reconstruction techniques, our approach can restore DIC images from various shear directions. As qualitatively and quantitatively proved by our experiments, restoration from multiple shear directions can decrease the ambiguity among different individual restorations. The restored DIC images are directly proportional to specimen's physical measurements without the pseudo 3D effect, which is very amenable for microscopy image analysis such as cell segmentation.

Acknowledgements

References

1. Arnison, M., Larkin, K., Sheppard, C., Smith, N., Cogswell, C.: Linear phase imaging using differential interference contrast microscopy. J. Microsc. 214, 7–12 (2003)
2. Arnison, M., Cogswell, C., Smith, N., Fekete, P., Larkin, K.: Using the hilbert transform for 3d visualization of differential interference contrast microscope images. J. Microsc. 199(1), 79–84 (2000)
3. Baraniuk, R.: Compressive sensing. IEEE Sig. Proc. Mag. 24(4), 118–121 (2007)
4. Besel, P., Mckay, N.: A method for registration of 3-d shapes. IEEE Trans. on Pattern Recognition and Machine Intelligence 14(2), 239–256 (1992)
5. Harris, C., Stephens, M.: A combined corner and edge detector. In: the 4th Alvey Vision Conference (1988)
6. Heise, B., Arminger, B.: Some aspects about quantitative reconstruction for differential interference contrast (dic) microscopy. In: ICIAM07 (2007)
7. Heise, B., Snnleitner, A., Klement, E.: Dic image reconstruction on large cell scans. Microscopy Research and Techniques 66, 312–320 (2005)
8. Kam, Z.: Microscopic differential interference contrast image processing by line integration (lid) and deconvolution. Bioimaging 6, 166–176 (1998)
9. King, S., Libertun, A., Piestun, R., Cogswell, C.: Quantitative phase microscopy through differential interference imaging. J. BioMed. Opt. 13, 024020 (2008)
10. Li, K., Kanade, T.: Nonnegative mixed-norm preconditioning for microscopy image segmentation. In: Information Processing in Medical Imaging (2009)
11. Munster, E., Vliet, L., Aten, J.: Reconstruction of optical path length distributions from images obtained by a wide-field differential interference contrast microscope. J. Microsc. 188, 149–157 (1997)
12. Murphy, D.: Fundamentals of Light Microscopy and Electronic Imaging. Wiley (2001)
13. Preza, C.: Rotational-diversity phase estimation from differential-interference-contrast microscopy images. J. of the Opt. Soc. of America A 17(3), 415–424 (2000)
14. Preza, C., Snyder, D., Conchello, J.A.: Theoretical development and experimental evaluation of imaging models for differential interference contrast microscopy. J. Opt. Soc. Am. A 16(9), 2185–2199 (1999)
15. Shribak, M., LaFountain, J., Biggs, D., Inoue, S.: Orientation-independent differential interference contrast (dic) microscopy and its combination with orientation-independent polarization system. J. Biomed. Opt. 13(1), 014011 (2008)
16. Yin, Z., Li, K., Kanade, T., Chen, M.: Understanding the optics to aid microscopy image segmentation. In: Medical Image Computing and Computer Assisted Intervention (2010)